Universiteit Antwerpen

Hybrid core–shell nanoparticles for cell-specific magnetic separation and photothermal heating

Hybrid Core-Shell Nanoparticles for Cell-Specific Magnetic Separation and Photothermal Heating

Cristina de la Encarnación[#,a,b], Felix Jungwirth[#,a,c], David Vila-Liarte[a,b,d], Carlos Renero-Lecuna[a,d], Safiyye Kavak[e], Iñaki Orue[f], Claire Wilhelm[g], Sara Bals[e], Malou Henriksen-Lacey[a,d], Dorleta Jimenez de Aberasturi*[,a,d,h], Luis M. Liz-Marzán*[,a,d,h]

Hyperthermia, as the process of heating a malignant site above 42 °C to trigger cell death, has emerged as an effective and selective cancer therapy strategy. Various modalities of hyperthermia have been proposed, among which magnetic and photothermal hyperthermia are known to benefit from the use of nanomaterials. In this context, we introduce herein a

hybrid colloidal nanostructure comprising plasmonic gold nanorods (AuNRs) covered by a silica shell, onto which iron oxide nanoparticles (IONPs) are subsequently grown. The resulting hybrid nanostructures are responsive to both external magnetic fields and near-infrared irradiation. As a result, they can be applied for the targeted magnetic separation of selected cell populations – upon targeting by antibody functionalization – as well as for photothermal heating. Through this combined functionality, the therapeutic effect of photothermal heating can be enhanced. We demonstrate both the fabrication of the hybrid system and its application for targeted photothermal hyperthermia of human glioblastoma cells.

10th Anniversary Statement

Luis Liz-Marzán has been an author in The *Journal of Materials Chemistry* since 2000, he was also a guest editor of a special issue in 2006, soon after entering the Editorial Advisory Board. After the journal splitting in 2013, Liz-Marzán continued being in the EAB of The *Journal of Materials Chemistry B*. We have naturally continued publishing our work in the journal and are happy to be part of the 10th anniversary celebration. HAPPY BIRTHDAY!

Introduction

The development of minimally invasive cancer treatments is of great interest, toward reducing the worldwide burden of cancer-associated morbidity and mortality.[1] Tumour ablation via hyperthermal processes is one of the methods being explored, aiming to cause local and intense heating of cancerous tissue to temperatures above 42 °C, thereby resulting in the initiation of cell death associated mechanisms, such as apoptosis and necrosis.[2] Among the various methods available to induce hyperthermia, the use of noble metal plasmonic nanoparticles (NPs) as sensitizers for photothermal heating has raised significant interest. When irradiated with a laser wavelength matching a localized surface plasmon resonance

(LSPR) mode in the NPs, part of the absorbed photon energy is converted into heat and released to the nearby environment. As a result, rapid heating can be achieved, radiating from the NPs location. Another interesting feature of plasmonic NPs is the possibility of tuning the LSPR wavelength through geometrical parameters (size and shape). For example, in gold nanorods (AuNRs), the longitudinal LSPR absorbance band can be tuned into the near infrared (NIR) region, where human tissue is most transparent, allowing for selective heating of the nanostructures with negligible harm to healthy tissue when a NIR laser is used.[3] The efficacy of such photothermal heating (PTH) is thus dependent on properties associated with the laser (intensity, duration, etc.), the tissue (refractive index, heat-sink effects, etc.), and the morphological properties of the gold NPs (AuNPs), including their LSPR wavelength, concentration, and stability in biofluids.

In addition to AuNPs, magnetic iron oxide NPs (IONPs) based on either magnetite (Fe_3O_4) or maghemite (γ-Fe_2O_3), have also shown promise as nanoheaters, by magnetic hyperthermia.[4] In contrast to plasmonic NPs, the method of heat induction is fundamentally different in this case, involving the dissipation of magnetic energy by hysteresis losses and/or Neel or Brown relaxation, upon exposure to high frequency alternating magnetic fields.[5] Besides thermal therapeutic applications, both AuNPs and IONPs can be used in a wide variety of diagnostic imaging applications, for example AuNPs are useful in computed tomography (CT), photoacoustic imaging (PAI), or surface-enhanced Raman scattering (SERS), whereas IONPs are excellent contrast agents for magnetic resonance imaging (MRI). Each technique offers differing levels of resolution, contrast, penetration depth, and ultimately feasibility for their use in clinical settings. Therefore, the combination of both materials in single NP entities, thus forming hybrid NPs, is of great interest to maximise the multimodal and correlative nature of such systems.[4] Indeed, not only can multiple imaging modalities be combined (i.e. MRI and SERS),[6] but also diagnostic and therapeutic applications, resulting in the commonly used term of theranostics.[7] Finally, the elemental components of such hybrid NPs offer a wide range of supplementary applications, such as magnetically controlled cell separation[8,9] or heat-induced drug delivery,[3] both of which could be included to achieve a truly multimodal hybrid NP system.

Whereas most of the literature relating to hybrid magnetic-plasmonic NPs in biomedical applications has been based on using IONPs covered by a gold shell,[10,11] we chose to explore a reverse NP construction, in which a gold core is surrounded by IONPs. By working with pre-synthesized Au NPs, a better control can be achieved over the LSPR, which is essential for PTH. AuNR synthesis in which the longitudinal LSPR maximum can be tailored to the wavelength of interest is well documented.[12] Subsequent growth of IONPs on the outer surface of the hybrid NPs provides accurate control over their coverage, via sequential thermal decomposition steps, which could not be realized were the IONP located in the hybrid NP interior. We thus propose a core-shell structure comprising an AuNR core – sensitive to NIR irradiation – coated with a silica shell, on which small IONPs are firmly adsorbed to allow for magnetic separation. Both components could additionally be used in various other bio-applications related to theranostics, such as magnetic resonance imaging (MRI), computed tomography (CT), or photothermal drug release. NPs can also be targeted through surface functionalization, and herein we further demonstrate the possibility for targeted PTH by functionalizing the hybrid NPs with antibodies against the cell membrane CD44 protein, a key receptor for hyaluronic acid that is involved in biological processes such as cell–cell interactions, cell adhesion, migration, and, crucially, tumour metastasis.[13] As a model cell type we employed human glioblastoma cells, but the technique could be used for any other CD44-expressing cells, and equally other receptors could be targeted by using the corresponding antibodies.

Results and discussion

Synthesis and characterization of hybrid nanoparticles

The fabrication of multifunctional hybrid NPs involves multiple synthetic steps. AuNRs were synthesized by means of a standard seeded-growth method[12] and subsequently coated with mesoporous silica shells,[14] which provided stability as well as surface silanol groups that could be used for further functionalization. Then, magnetic IONPs were directly grown onto the silica shells, through a stepwise thermal decomposition of organometallic iron precursors.[15]

The synthesis of IONPs on top of SiO_2 NPs required selection of the appropriate IONP density on the silica surface, through the number of thermal decomposition steps. Therefore, we first carried out an optimization process, using mesoporous SiO_2 NPs of 150 nm and 240 nm diameter, synthesized using the same modified Stöber method,[14] but in the absence of the AuNR cores. The growth of IONPs on the SiO_2 NPs surface involved the thermal decomposition of iron oleate, as reported by Nistler et al.[16] Briefly, mesoporous silica particles in ethanol were mixed with iron (III) oleate dissolved in 1-octadecene. Oleic acid, which acts as a stabilizing agent, was then added, the mixture was heated at a controlled rate of 200 ºC/h, and then maintained at 317 ºC for 30 min, to promote iron oleate decomposition and formation of IONPs. To obtain the final product, the reaction mixture was centrifuged to separate IONP-decorated silica (SiO_2@IONPs) from free IONPs in the reaction medium. The IONP coverage on SiO_2 NPs was gradually increased for an increasing number of thermal decomposition steps (up to five). A schematic representation of the synthesis is shown in **Figure S1A** (Supplementary Information, SI). The resulting SiO_2@IONPs were imaged by TEM, observing that the density and size of IONPs could be gradually increased by increasing the number of thermal decomposition steps (**Figure S1B**).

Although the synthesis was successful for both 150 and 240 nm SiO_2 particles, we selected the smaller ones for magnetic characterization because of their higher specific surface area. Hysteresis loops and zero field cooled/field cooled (ZFC/FC) curves were recorded, and the results are shown in **Figure S2**. We first measured the magnetic properties of those SiO_2@IONPs with the lowest IONP density, i.e., those obtained from a single thermal decomposition step (SiO_2@1IONPs). The hysteresis loop (M(H)) for this sample (**Figure S2A**) shows a high saturation magnetization of 75 emu/g, in agreement with values reported in the literature.[17] These results indicate a superparamagnetic behaviour for SiO_2@1IONPs, with low remanence and coercivity, which was found to lower further when increasing the number of thermal decomposition steps (**Figure S2B**). This behaviour was confirmed by the ZFC/FC curves for both samples. The blocking temperature, estimated as the point where the ZFC curve exhibits an apex, was determined to be $T_B = 100$ K, but shifted to $T_B = 225$ K for a higher number of decomposition steps (**Figure S2C,D**). Analysis of the normalized magnetization M/Ms (H) at 300 K according to the Langevin model[18] (see Experimental Section) and fitting of ZFC/FC measurements, yielded a size (diameter) distribution centred around 10 nm in SiO_2@1IONPs (one growth step).

Fitting of ZFC/FC measurements for SiO$_2$@4IONPs was performed using the same parameters (magnetization, thermal dependence etc.) as those for SiO$_2$@1IONPs, for meaningful comparison. The estimated average size in this case was 15 nm, thereby confirming NP growth. The 3D structure of the SiO$_2$@IONPs was characterized by electron tomography (**Figure S3**). Additionally, the ZFC curve indicates that IONPs are made of maghemite (γ-Fe$_2$O$_3$), due to the absence of a shoulder near 110 K, which is known to correspond to a peculiar metal-insulator transition in Fe$_3$O$_4$.[19] The SiO$_2$@IONPs could be efficiently separated by placing a hand-held magnet near the solution, resulting in NP accumulation into a pellet. We observed that SiO$_2$@IONPs with a lower density of IONPs were difficult to separate magnetically, whereas those synthesized with 3-5 thermal decomposition steps were readily separated. However, whereas SiO$_2$@3IONPs and SiO$_2$@4IONPs were easily redispersed upon removal of the magnet, SiO$_2$@5IONPs remained as a hard pellet.

Once the growth of IONPs on the surface of silica particles was optimized, the method was implemented for hybrid NPs including AuNRs as plasmonic cores. A schematic representation of the complete process is shown in **Figure 1A**. AuNRs were synthesized by a three-step seed-mediated method,[9] involving the controlled growth of pre-made AuNR seeds (7.5 nm x 21.0 nm) into larger AuNRs (16.4 ± 2.7 nm x 66.5 ± 5.7 nm) with a longitudinal LSPR at 790 nm (**Figures 1B** and **S4**). AuNRs were then coated with a mesoporous silica shell using a modified Stöber method.[14] Briefly, a colloidal dispersion containing AuNRs, CTAB, ethanol, and water was prepared. After adjusting the pH to 9 by addition of aqueous ammonia, a selected amount of tetraethyl orthosilicate (TEOS) was added dropwise under strong stirring, to trigger TEOS hydrolysis and SiO$_2$ condensation. After TEOS addition, the temperature was increased to 60 °C and the mixture was stirred for three days. Then, the particles were recovered by centrifugation and thoroughly washed with ethanol and dilute HCl, to remove the surfactant (CTAB). Normalized UV-vis spectra and TEM images were recorded for initial characterization (**Figures 1C and S4**). The TEM images showed uniform encapsulation of every AuNR by a silica shell, with a thickness of 70.8 ± 8.2 nm, while the UV-Vis spectrum showed a small redshift of the longitudinal LSPR, as expected for an increased local refractive index upon silica deposition.

Finally, IONPs were grown on the silica surface by using the procedure optimized for SiO$_2$@IONPs. In short, AuNR@SiO$_2$ NPs were added to a solution of oleic acid and iron (III) oleate in 1-octadecene, followed by controlled temperature increase, leading to the decomposition of the iron complex and formation of AuNR@SiO$_2$@IONPs, which were recovered and washed by centrifugation. The thermal decomposition step was repeated up to three times to increase IONP surface coverage, yielding densely covered hybrid NPs (**Figure S5A1-3**). It should be noted that, as found in an initial optimization process using AuNRs with an LSPR at 760 nm, the thermal treatment induced partial shortening of AuNRs, with a corresponding LSPR blueshift to 730 nm (**Figure S5B**). Therefore, we chose to compensate for AuNR reshaping by initially using longer AuNRs (16.4 ± 2.7 nm x
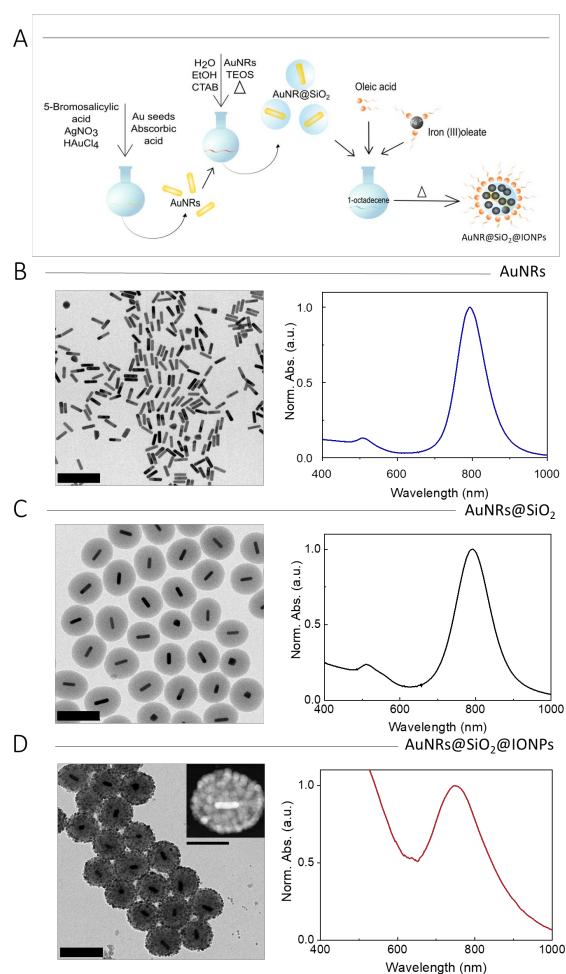

Figure 1. (A) Schematic representation of the synthesis of AuNR@SiO$_2$@IONPs. (B-D) TEM images and normalized (at LSPR maximum) UV-Visible spectra for AuNRs (B), AuNR@SiO$_2$ (C), and AuNR@SiO$_2$@IONPs (D). The inset in (D) shows a single particle imaged using high-angle annular dark field (HAADF) STEM. Scale bars correspond to 200 nm (100 nm in the inset).

66.5 ± 5.7 nm) with a longitudinal LSPR at 790 nm. By using an optimized number of three decomposition steps, dense and homogenous IONP coverage was achieved. The 3D structure was confirmed by electron tomography (**Figure S6**). Representative results of TEM and UV-vis spectroscopy characterization are shown in **Figure 1D**. It should be noted that the colloidal stability of these NPs decreased for higher IONP loadings. When comparing the UV-vis spectra of AuNRs and AuNR@SiO$_2$ (**Figure 1B,C**) with that of AuNR@SiO$_2$@IONPs (**Figure 1D**) a significant LSPR blue shift from 790 to 760 nm was observed, in agreement with partial thermal AuNR reshaping at the high temperature employed for IONP formation.[20,21] This AuNR shortening effect also became apparent in TEM images, the initial AuNRs appeared longer (66.5 ± 5.7 nm length, 16.4 ± 2.7 nm width, 4.1 aspect ratio) than the final AuNRs (58.3 ± 5.1 nm length, 15.1 ± 2.4 nm width, 3.8 aspect ratio). In the final sample, the AuNR LSPR bands show an apparent damping
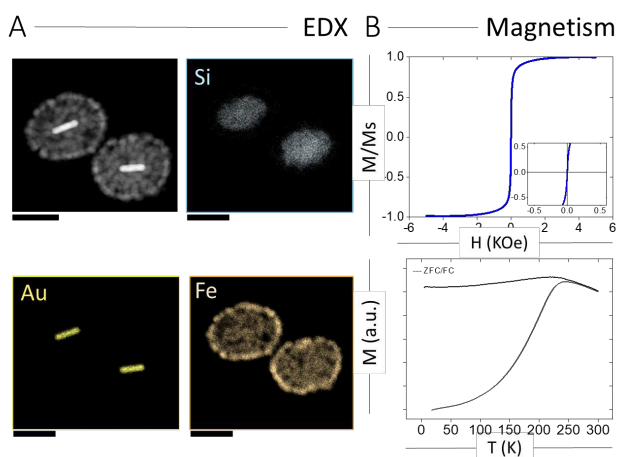
Figure 2. (A) EDX analysis of AuNR@SiO$_2$@IONPs, showing the elemental distribution of Au, Fe and Si. Scale bars correspond to 100 nm. **(B)** Hysteresis loop and ZFC/FC curves for AuNR@SiO$_2$@IONPs. The inset in **(B)** shows a magnification of the central area of the curve, in which coercivity and remanence are appreciated to be negligible.

caused by the high background signal produced due the presence of IONPs, which shows as a broad shoulder rising into the UV region.[22]

Upon completion of the synthetic process, the external layer of oleate-capped IONPs renders the hybrid AuNR@SiO$_2$@IONPs hydrophobic. However, for their use in biological environments, stability in aqueous media is required. Therefore, an additional phase transfer step was carried out, through encapsulation with an amphiphilic polymer.[23,24] Dodecylamine-modified polyisobutylene-alt-maleic anhydride (PMA) was employed for

the encapsulation of both AuNR@SiO$_2$@IONPs and SiO$_2$@IONPs, the latter to be used as controls in subsequent experiments. No phase transfer was required for AuNRs@SiO$_2$ (also used as a control in some experiments) because these particles were readily stable in polar solvents after synthesis. However, AuNR@SiO$_2$ were functionalized with a polyethylene glycol (PEG)-silane of a similar size as PMA, to enhance their stability and to mimic the coating of AuNR@SiO$_2$@IONPs. These coatings allowed us to study the hybrid NPs and their controls (AuNR@SiO$_2$ and SiO$_2$@IONPs) under similar conditions. The detailed procedure is described in the Experimental Section.

The spatial elemental distribution of Au, Si, and Fe in the hybrid NPs was characterized using energy dispersion X-ray spectroscopy (EDX) analysis in electron microscopy. As shown in **Figure 2A**, all three components were observed at their expected locations (AuNRs inside the silica shell and IONPs on the outer silica surface). We also characterized the magnetic properties of AuNR@SiO$_2$@IONPs, and the corresponding hysteresis loop and ZFC/FC curves are plotted in **Figure 2B**. Again, the hysteresis loop revealed a superparamagnetic behaviour at room temperature, with no remanence and low coercivity. On the other hand, the ZFC/FC curves showed a
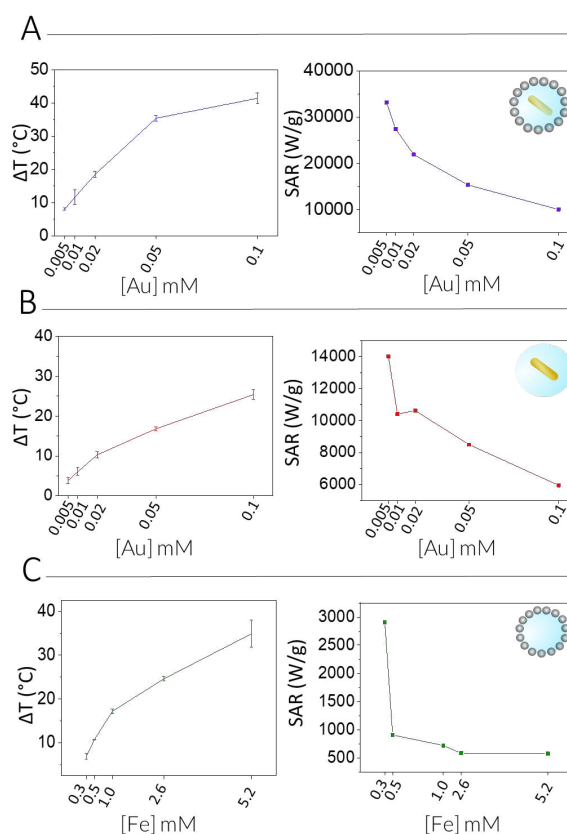

Figure 3. Average PTH temperature increase (ΔT, °C) and estimated SAR, using conditions of 5 min irradiation (808 nm) at 2.5 W/cm^2 in solution, at different concentrations of AuNR@SiO$_2$@IONPs **(A)**, AuNR@SiO$_2$ **(B)**, and SiO$_2$@IONPs **(C)**. Results show mean ± SD of triplicate measurements (error bars for SAR are within the symbols).

Table 1. Average temperature increment (ΔT) for PTH under 808 nm and 5 min irradiation at 2.5 W/cm^2, for colloidal dispersions of AuNR@SiO$_2$ (red), SiO$_2$@IONPs (green), and AuNR@SiO$_2$@IONPs (blue), at different metal concentrations.

[Au] mM	ΔT (°C)	[Fe] mM	ΔT (°C)	[Au] mM	[Fe] mM	ΔT (°C)
0.005	3.8 ± 0.8	0.3	6.9 ± 0.7	0.005	0.3	8.0 ± 0.3
0.01	6.1 ± 1.0	0.5	10.7 ± 0.1	0.01	0.5	11.6 ± 2.1
0.02	10.3 ± 0.8	1.0	17.2 ± 0.5	0.02	1.0	18.5 ± 0.9
0.05	16.8 ± 0.5	2.6	24.6 ± 0.5	0.05	2.6	35.4 ± 0.8
0.1	25.4 ± 1.2	5.2	34.9 ± 3.1	0.1	5.2	41.4 ± 1.6

blocking temperature of 230 K, similar to that obtained for SiO$_2$@4IONPs (**Figure S2D**). Finally, the response of AuNR@SiO$_2$@IONPs to an external magnetic field was evaluated toward their use for rapid magnetic separation. To this end, an aqueous dispersion of AuNRs@SiO$_2$@IONPs was placed in an Eppendorf tube and a magnet placed at the side, resulting in fast magnetic separation and accumulation into a pellet at the tube wall within 20 s (**Figure S7**). Upon removal of the magnet, the NPs could be redispersed again in water and remained colloidally stable. The described separation process could be repeated for any desired number of times.

We next measured the PTH performance of the hybrid NPs using an 808 nm laser, which closely matches the LSPR maximum of the AuNRs. We chose to use a laser irradiation setup in which the spot size was matched to the sample diameter, thus allowing us to measure the true power density in the exposed sample area. Dispersions with different NP concentrations (measured using inductively coupled plasma mass spectrometry, ICP-MS) were irradiated for 5 min and temperature increments were registered using a NIR thermal camera, collecting data from a region of interest (ROI), corresponding to the NP dispersion. The absolute temperature was measured at different times and temperature increments were calculated by subtracting the initial temperature (time = 0) from the final temperature (time = 5 min) (**Figure 3**, left column, **Table 1**). The specific absorption rates (SAR), which represent the power absorbed per mass of material,[25] were also calculated (**Figure 3**, right column). Specific measurement details can be found in the Experimental Section. As expected, for each system, an increase in temperature was observed with increasing NP concentration (as expressed in [Fe], [Au], or OD$_{808}$), although it was found not be linear because of light attenuation at higher concentrations.

Through comparison across the different NP systems, we observed that, for a certain concentration of Au and or Fe in AuNR@SiO$_2$@IONPs, the equivalent control samples resulted in weaker heating, and that the AuNR@SiO$_2$ control consistently heated less than the SiO$_2$@IONPs. In other words, at comparable concentrations, the presence of both metals always resulted in a cumulative heating. Indeed, recently it was shown that iron oxide nanomaterials could be efficient nano-heaters in the NIR, where an absorption band can be assigned to an intervalence charge transfer between Fe^{3+} and Fe^{2+} cations.[26] Besides, under the conditions studied, the contribution of iron
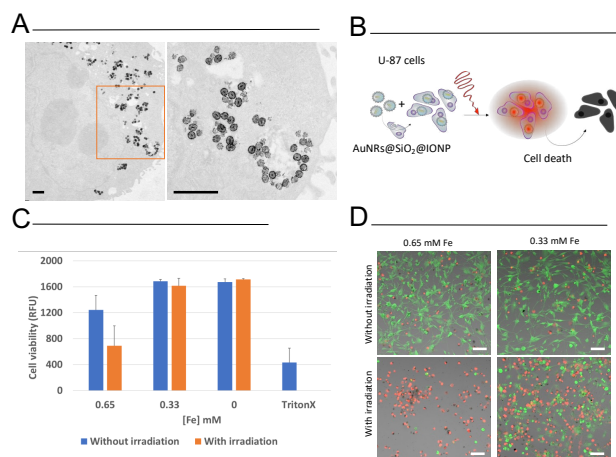

Figure 4. (A) TEM images of U87 cells exposed to AuNR@SiO$_2$@IONPs for 24h. The right-hand image corresponds to the area highlighted by an orange box in the left-hand image. Scale bars: 1 µm. **(B)** Schematic illustration of biological PTH. **(C)** U87 cell viability after exposure to AuNR@SiO$_2$@IONPs for 24h, followed by irradiation with an 808 nm laser. The relative fluorescence intensity (RFU), a measure of cell viability is shown after additional 24h, determined using the Alamar Blue assay. Mean ± SD of triplicate measurements. **(D)** Live/Dead fluorescence imaging of cells 5 days post irradiation, showing dead cells in red (propidium iodide) and live cells in green (Calcein). Scale bars: 100 µm.

oxide is found higher than that of gold due to the higher proportion of IONPs versus AuNRs per hybrid particle (see the difference in global Fe versus Au concentration). Upon a recalculation taking the relative concentrations into account, it clearly shows that AuNRs remain much more efficient heaters, as expected from the presence of an LSPR mode in close resonance with the laser wavelength (808 nm vs. LSPR@760 nm). From these calculations, we estimate that 25 times more Fe in SiO$_2$@IONPs compared to Au in AuNRs@SiO$_2$ was needed to reach the same temperature increment. We attempted to relate these heating properties based on the optical density (OD$_{808}$) due to the different NPs. However, taking into consideration the significant differences in metal concentration, that the maximum OD of Fe is not at 808 nm, and that the sum of both metals does not result in a sum of OD, such a comparison was difficult to make (**Table S1**).

Biological application of hybrid nanoparticles

Biological assays were carried out using a human glioblastoma cell line, U87. We first screened cell viability upon exposure to AuNR@SiO$_2$@IONPs for 24h and 48h (**Figure S8**). At concentrations ranging between 0.16 and 1.3 mM [Fe] (corresponding to 3 – 25 µM [Au]), no cytotoxicity was observed after 24h. However, after a further 24h (total of 48h) significant cytotoxicity at the highest concentrations was observed. We thus chose to work with 0.33 and 0.65 mM [Fe] (6.3 and 12.5 µM [Au]) for further cell studies, i.e., incubating U87 cells with AuNR@SiO$_2$@IONPs for 24h followed by removal of any non-

endocytosed fraction. Brightfield imaging showed high levels of uptake (**Figure S8C**), corroborated by TEM analysis of NP uptake after 24h showing endosomal uptake (**Figure 4A**). Considering literature reports that claim increased photothermal effects when NPs have been internalized by cells,[25,27,28] we studied the heating efficiency of AuNR@SiO$_2$@IONPs upon cell internalization (**Figure 4B**). We subsequently proceeded to irradiate the samples (see Experimental section for full details), evaluating biocompatibility by using the Alamar Blue cell viability assay, immediately post irradiation and after a further 24h, and by using live/dead fluorescence labelling up to 5 days post irradiation (**Figure 4C, D; Figure S9**). The results show that PTH induces cytotoxicity in a time-dependent manner, suggestive of apoptosis or ferroptosis cell death mechanisms, as previously documented in other works.[29–31] Furthermore, considering that the photothermal component of AuNR@SiO$_2$@IONPs (i.e., AuNR) is in relatively low concentration compared to the Fe component (52-fold less Au than Fe), high laser power densities were required to observe efficient PTH-induced cell death.

As it is well known that 2D cell cultures have severe limitations to reproduce the real biological environment, 3D models have become a more reliable testbed to evaluate cell behaviour under different conditions.[32] Therefore, we used a 3D model to further evaluate the PTH properties of our NPs in a more realistic scenario. Under certain growth conditions, U87 cells spontaneously form cell spheroids, which can be used as miniaturized 3D models for high-throughput testing. U87 cells were incubated for 24 h with AuNR@SiO$_2$@IONPs (0.33 and 0.65 mM [Fe], equivalent to 6.3 and 12.5 µM [Au], respectively) in 2D cell growth substrates, and subsequently transferred to spheroid microplates to obtain an array of spheroids placed at the same imaging plane. After 72 h, spheroids were collected into an Eppendorf tube and irradiated for 5 min. After irradiation, spheroids were transferred back to spheroid microplates for subsequent imaging using Live/Dead fluorophores, to evaluate the extent of cell death (**Figures 5 and S10**). Controls were used to confirm the non-toxic nature of the NPs in spheroids, in addition to the lack of induced cell death upon irradiation of spheroids without NPs. Regarding NP-exposed spheroids, we again found a time-dependent increase in cell death upon irradiation, studied up to 48h post irradiation. As observed here and widely reported in the literature, NPs are readily uptaken by cells, even if they do not carry any specific surface-targeting ligands.[24] If specific cancer cell targeting is to be achieved, NPs should be conjugated with antibodies (or other biorecognition elements), so that intracellular uptake would be limited by specific antibody-antigen receptor interactions at the cell membrane.[33] For this study we chose to target the transmembrane glycoprotein CD44, a commonly expressed receptor in various cancer types and especially upregulated in metastatic tumour cells.[34] U87 can be effectively targeted using anti-CD44 molecules, thanks to its ubiquitous membrane expression.[35] Functionalization of AuNR@SiO$_2$@IONPs with antibodies was performed using a protocol based on the activation of free carboxylic groups in the PMA structure, via 1-Ethyl-3-(3-
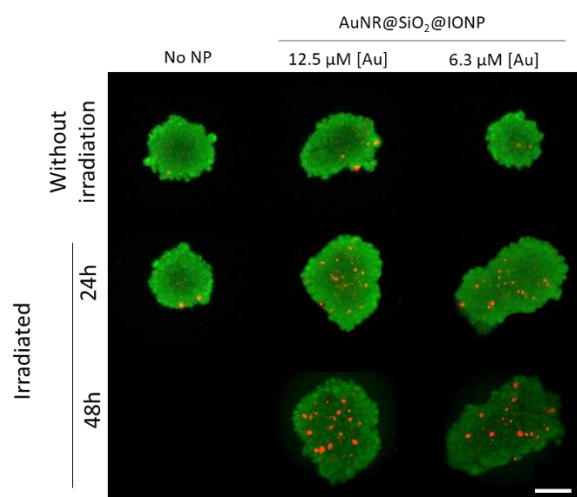

Figure 5. Live/Dead images of spheroids in which cells were pre-incubated with AuNR@SiO$_2$@IONPs (6.3 and 12.5 µM [Au], equivalent to 0.33 and 0.65 mM [Fe], respectively) prior to forming spheroids. Irradiations were for 5 min using an 808 nm laser, with cell viability determined 24 h and 48 h post irradiation. Scale bar: 100 µm. Additional examples of spheroids are shown in the SI (**Figure S10**).

dimethylaminopropyl)carbodiimide/N-hydroxysuccinimide (EDC/NHS) chemistry,[36] and subsequent binding of an anti-human anti-CD44 antibody via protein G (see Experimental Section). The use of protein G assisted the correct orientation of the antibody, which maintained free its fragment antigen-binding region (Fab region), to interact with CD44 on the cell surface.

Immunostaining was first used to verify that U87 cells were positive for the expression of CD44. We explored the use of non-labelled, and Alexa Fluor (AF) labelled, antibodies both for this step and for conjugation to AuNR@SiO$_2$@IONPs. The experiments presented herein were conducted with AF488-labelled CD44 (DF1485), but other examples and alternatives are shown in the SI (**Figure S11**). Cells were grown as an adherent culture and fixed prior to normal direct immunostaining protocols. As can be observed in **Figure 6A**, U87 cells were positive for CD44 expression. We thus added AuNR@SiO$_2$@IONP-AB to cells and incubated for 2h, followed by washing to remove non-associated NPs and carry out live cell imaging. We examined the presence of NPs using both fluorescence (detecting AF488) and multiphoton (MP) confocal microscopy, the latter being used to detect the NPs directly. As shown in **Figure 6A**, both the fluorescence and MP signals correlated perfectly, confirming that MP confocal microscopy can be used to image NPs in live cells, thereby avoiding the requirement to fix and locate the NPs using immunostaining protocols when non-labelled antibodies are used. Similar surface expression of CD44 was observed by incubating the breast cancer cell line MDA.MB.231 with AuNR@SiO$_2$@IONP-AB, indicating that this system can work with multiple cell types (**Figure S12**). In all cases, adjusting NP concentration was crucial to avoid overloading: a concentration at 0.33 mM Fe (6.3 µM Au) gave good results. ICP-MS data suggests that ca. 70% of
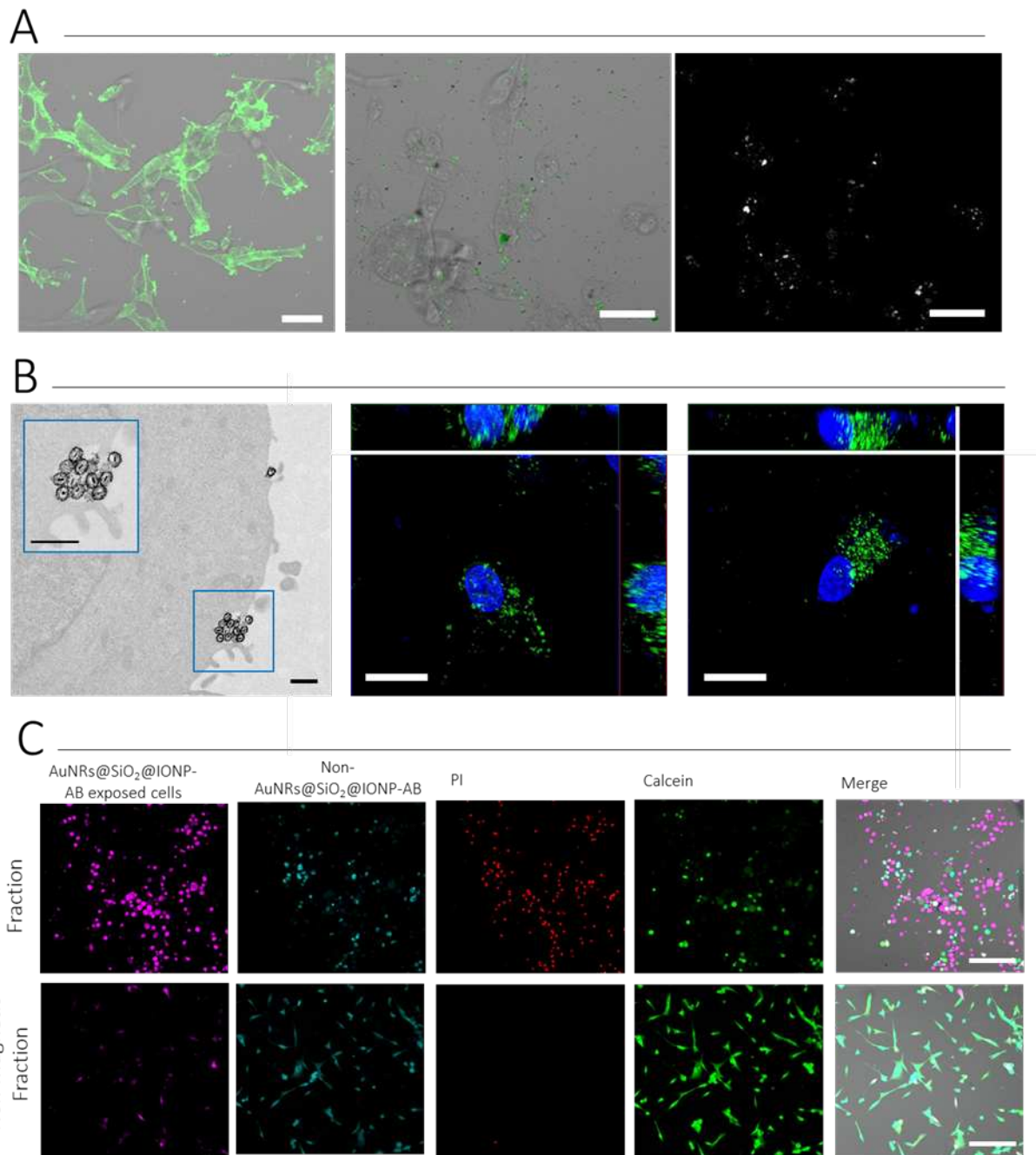
Figure 6. (A) Verification of CD44 expression on U87 cells (left), and subsequent AuNR@SiO$_2$@IONP-AB targeting of cells, viewed using brightfield and fluorescence detection of AF488 (centre), as well as multiphoton microscopy (right). Scale bar: 50 µm **(B)** AuNR@SiO$_2$@IONP-AB incubation with U87 cells for 2h results in surface binding, as observed via TEM (left) and fluorescence confocal microscopy (centre). In comparison with AuNR@SiO$_2$@IONPs (right), surface association is clearly observed. Scale bars 50 µm (TEM), 20 µm (confocal). **(C)** Fluorescence confocal microscopy showing magnetic separation of AuNR@SiO$_2$@IONP-AB associated with CD44 expressing cells, and subsequent PTH-induced cytotoxicity. Scale bars: 200 µm.

added AuNR@SiO$_2$@IONP-AB NPs were associated with cells, giving sufficient signal in both fluorescence and MP imaging to detect *in situ* the spatial location of the NPs (**Figure S13**). In contrast, AuNR@SiO$_2$@IONP added at the same concentration for also 2h resulted in ca. 10% association. Furthermore, we employed TEM imaging to verify the membrane location of AuNR@SiO$_2$@IONP-ABs, which was further corroborated by fluorescence confocal imaging (**Figure 6B**).

We subsequently proceeded to determine the suitability of CD44-targeted NPs for magnetic cell selection, followed by inducing cell death via PTH. U87 cells were divided into two groups, each labelled with a different fluorophore ("Cell

Tracker" fluorophores). Only one group was incubated with AuNR@SiO2@IONP-AB. Subsequently, both populations were mixed, and a magnet was placed in contact with the side of the Eppendorf tube. After 5 min, ca. 75% of the solution was carefully removed (herein termed "Non-Magnetic Fraction", taking special care to avoid the side in contact with the magnet. Both the non-magnetic fraction and the remaining "Magnetic Fraction" were analysed via fluorescence microscopy to determine the proportion of each cell population, and via ICP-MS to determine the proportion of AuNR@SiO2@IONP-AB in each fraction. Upon confirmation of successful separation of the cells exposed to AuNR@SiO2@IONP-AB in the Magnetic Fraction, we proceeded to irradiate both fractions with an 808 nm laser, followed by Live/Dead staining the following day, to determine PTH-induced cytotoxicity. As can be seen in **Figure 6C**, very few AuNR@SiO2@IONP-AB expressing cells (those in pink) were imaged in the non-magnetic fraction in agreement with the high level of magnetic cell separation. Indeed, ICP-MS analyses of both the Magnetic and Non-Magnetic fractions suggest that the efficiency of magnetic separation is close to 75 %. Regarding the ability to cause PTH-induced cytotoxicity, PI-expressing cells (dead cells) were only observed in the Magnetic Fraction (pink fraction), as expected because this was the cell population containing hybrid NPs. We additionally noted that, the cell morphology was drastically different in both fractions, indicating that the irradiated Magnetic Fraction was indeed non-viable whereas the irradiated Non-Magnetic fraction was composed of viable cells (due to the lack of hybrid NPs in this fraction which can cause PTH). Taken together, these results suggest that PTH results in the specific death of only those cells containing AuNR@SiO2@IONP-AB, thereby confirming the suitability of the AB-labelled hybrid NPs for CD44 targeting, cell separation, and subsequent PTH-induced cytotoxicity protocols.

Conclusions

A multistep method was developed for the synthesis of hybrid, multifunctional NPs. Starting from AuNRs and silica coating, IONPs were grown using thermal decomposition of iron oleate. The density of IONPs on the silica surface can be increased by performing multiple thermal decomposition steps, which number was optimized using core-free SiO2 NPs. Electron microscopy confirmed that the number of decomposition steps could be used not only to tailor surface coverage, but also the size of IONPs, which reached 19 nm after 3 thermal decomposition steps. We hypothesize that, IONPs are formed in the first step and then act as nucleation and preferential growth sites for subsequent steps.

The obtained AuNR@SiO2@IONPs were characterized by TEM, HAADF and EDX, thereby confirming the structure and composition of the hybrid NPs. UV-Vis spectra were also recorded, showing partial reshaping of AuNRs due to the high temperature used during IONP synthesis. Additionally, magnetic characterization showed superparamagnetic behavior, characterized by low remanence and coercivity. The photothermal characterization of the NPs displayed promising properties as nanoheaters, achieving high temperature increments, even for low Au concentrations. By comparing with suitable controls and considering the molar concentration of each element, the heating capacity of AuNRs is ca. 25 times higher. The hybrid NPs were shown to induce PTH-based cytotoxicity in both 2D and 3D cell cultures, and their magnetic properties allowed the magnetic selection of cells. Specific targeting of CD44-expressing cancer cells was achieved by conjugating the corresponding antibodies to the AuNR@SiO2@IONPs surface. This strategy, in combination with magnetic selection and PTH, proves the suitability of these hybrid NPs as a potential cancer therapeutic method. A future interesting direction might take advantage of the hydrophobic drug loading ability of mesoporous silica, thus creating a heat-sensitive drug-release sponge.[37]

Experimental

Materials.

Ferric chloride hexahydrate (FeCl3·6H2O, ≥98%), sodium oleate (≥99%), ammonia (≥99.5%,), absolute ethanol (CH3CH2OH,), tetraethyl orthosilicate (TEOS), hexane (≥95%), 1-octadecene (≥90%), hexadecyltrimethylammonium bromide (CTAB, ≥99%), 1-decanol (98%), hydrogen tetrachloroaurate trihydrate (HAuCl4·3H2O, ≥99.9%,), sodium citrate tribasic dihydrate (≥98%), silver nitrate (AgNO3, ≥99%), L-ascorbic acid (AA, ≥99%), O-[2-(3-mercaptopropionylamino)ethyl]-O'-methylpolyethylene glycol (SH-PEH,), 1-Ethyl-3-(3-dimethylaminopropyl)-carbodiimide (EDC, ≥98%), N-Hydroxysuccinimide (NHS, ≥98%), Phosphate buffered saline (PBS), Phosphate buffer (PB), 2-(N-morpholino)ethanesulfonic acid (MES buffer) were purchased from Sigma-Aldrich and COOH-PEG-silane (Mw 5000 Da) was purchased from Nanocs. All the reactants were prepared and used without further treatments. Milli-Q water was used for all the experiments.

Nanoparticle synthesis.

Synthesis of AuNRs. For the preparation of AuNRs, a seed-mediated method was used. Thus, first we have synthesized small AuNRs as seeds that were subsequently overgrown as bigger AuNRs.

Synthesis of small anisotropic seeds (L=21 nm W= 7.5 nm). Typically, 2400 μL of 0.01 M AgNO3, 21 mL of 1 M HCl, 3000 μL of 0.05 M HAuCl4, and 3900 μL of 0.1 M ascorbic acid were added to 300 mL of a 50 mM CTAB and 11 mM n-decanol solution at 25 °C. Then, 18 mL of the seed solution was added under stirring. The mixture was left undisturbed for at least 4 h at 25 °C. The obtained small anisotropic seeds displaying an LSPRs band located at 725-730 nm were centrifuged at 14000–15000 rpm for 45 – 60 min in 2 mL tubes. The precipitates were collected and diluted with 20 mL of a 10 mM CTAB solution. The AuNRs dispersion was centrifuged twice under the same conditions. The final volume of small AuNRs dispersion was fixed to [Au] = 4.6 mM.

Synthesis of AuNRs with LSPRs at 790 nm. In a typical synthesis, 2500 µL of a 0.01 M $AgNO_3$ solution, 1000 µL of 0.05 M $HAuCl_4$, 800 µL of a 0.1 M ascorbic acid solution and 3000 µL of HCl 1M were added under stirring to 100 mL of a 50 mM CTAB and 11 mM n-decanol solution at 28 °C. Then, 650 µL of the small anisotropic seed suspension was added. The mixture was left undisturbed for 12 h. The obtained AuNRs were centrifuged at 7000 rpm and dispersed in 10 mL of 2 mM CTAB solution. This process was repeated twice. AuNRs of 58 ± 5.1 nm in length and 15 ± 2.4 nm in width were obtained. The dimensions were directly measured by TEM and a maximum absorbance at 790 nm was determined from UV-Vis spectra.

Synthesis of core-shell AuNRs@SiO_2. The reaction was performed according a reported protocol.[13] 170 mL of a 6 mM CTAB solution and 75 mL of ethanol were mixed at a temperature between 30 and 35 °C in a 500 mL round beaker. Then, 100 µL of NH_3 (25 vol %) was added to the mixture, followed by addition of 5 mL of AuNRs 5 mM. Thereafter, 200 µL of TEOS was added dropwise under vigorous stirring. For the rest of the reaction time, the temperature was fixed at 60 °C. After 2–3 hours, the sample became gradually turbid indicating the formation of the silica shell. The final AuNRs@SiO_2 were recovered by centrifugation (9000 rpm, 20 min, 35 ºC) and washed twice with ethanol.

Synthesis of SiO_2 NPs. 350 mL of 6 mM CTAB and 150 mL of ethanol were mixed in a 1 L round bottom flask under mechanical stirring at 35 ºC. Then, the pH was adjusted to 9.5 by addition of NH_3 (5 wt%) and the mixture was stirred for 30 min. Afterwards, 3 mL of TEOS was added dropwise under vigorous stirring, thus, primary nucleation clusters are formed, then, the mixture turned turbid indicating the formation of the NPs. After 5 min, the temperature was set at 60 ºC and the reaction mixture was left for three days. The product was recovered by centrifugation (9000 rpm, 30 min, 35 °C), washed twice with ethanol and dried at 60 ºC in the oven. Finally, the NPs were calcined (4 h – 600 ºC) to clean completely the surface and to increase the stability.

Synthesis of SiO_2@IONPs. The obtained mesoporous silica NPs were covered with IONPs via thermal decomposition of iron (III) oleate, according to a protocol published by Park et al.[14] First, iron (III) oleate was prepared by dissolving 36.5 g sodium oleate and 10.8 g $FeCl_3 \cdot 6\ H_2O$ in a mixture of 60 mL water, 80 mL ethanol and 140 mL hexane and heating to reflux (ca. 70 °C) for 4 h. After cooling down, the organic layer was separated and washed four times with 60 mL water, the solvent was then evaporated and the product was dried, first using a rotary evaporator and then using a high vacuum line. After drying for 12 h, a dark orange viscous product was obtained, which was stored under argon and light exclusion.

To perform the thermal decomposition, 3 g of iron(III) oleate was dissolved in 21 mL of 1-octadecene in a 3 neck 150 mL round bottom flask equipped with a magnetic stirring bar. The reaction vessel was connected to a vacuum line and the mixture was degassed at 70 °C in a bath for 30 min. Afterwards, the

water bath was removed, and the flask was equipped with a reflux condenser, a thermocouple and a septum while applying a N_2-flow. 130 mg of mesoporous silica was dispersed in 3 mL of ethanol using a sonication bath and then added to the reaction mixture together with 535 µL of oleic acid. The flask was equipped with a septum and a thermocouple, and the reaction mixture was heated to 317 °C with a heating ramp of 200 °C/h and a holding time at 317 °C of 30 min. During the whole heating process, a gentle N_2-flow was applied, furthermore the water cooling for the reflux condenser was only switched on when the reaction reached a temperature of 200 °C, ensuring that all ethanol was removed from the reaction, which otherwise could drip back into the hot solvent causing splashing of the reaction mixture due to spontaneous evaporation. After cooling to room temperature, hexane was added and the product was recovered by centrifugation (9000 rpm, 10 min, 20 °C). The product was washed several times with hexane to remove unbound IONPs. For overgrowth, the same process was employed. First 130 mg of the prepared NPs was dissolved in 7 mL of 1-octadecene and then added to 3 g iron (III) oleate dissolved in 14 mL 1-octadecene. The mixture was degassed for 30 min, the flask was equipped with a reflux condenser and 535 µL of oleic acid was added. Then the same heating ramp was used, and the product was collected via centrifugation (9000 rpm, 10 min, 20 °C) and washed several times with hexane. This process was repeated until the desired coverage was obtained.

Synthesis of AuNR@SiO_2@IONPs. The growth of IONPs onto silica shells was performed through thermal decomposition. For this process, 1.2 g iron (III) oleate, prepared as described above, was dissolved in 10 mL of 1-octadecene in a 50 mL 3 neck round bottom flask equipped with magnetic stirring. The flask was connected to the high vacuum line and degassed at 70 °C bath temperature for 30 min. Afterwards the flask was equipped with a reflux condenser, a thermocouple and a septum while applying a N_2-flow. 15 mg AuNRs@SiO_2 in 1 mL ethanol and 267.5 µL oleic acid were added and the reaction mixture was heated to 317 °C with a rate of 200 °C/h under a weak N_2-flow, where it was held for 10 min. After cooling, hexane was added to the reaction mixture and the particles were recovered by centrifugation (9000 rpm, 10 min, 20 °C). The obtained product was washed several times with hexane yielding a slightly reddish dispersion. For overgrowth, the same process was employed. The dried particles were first dispersed in 5 mL of 1-octadecene which was added to 1.2 g iron (III) oleate. When drying the particles, precaution must be taken to not leave them without solvent for too long since the particles then become hard to disperse again. The obtained mixture was degassed at 70 °C bath temperature for 30 min. Afterwards 267.5 µL oleic acid was added and the reaction mixture was heated to 317 °C with a ramp of 200 °C/h under a weak N_2-flow. After cooling, hexane was added and the product was recovered by centrifugation (9000 rpm, 10 min, 20 °C). The obtained product was washed several times with hexane until the supernatant

remained clear. This process was repeated until the desired coverage was obtained.

Functionalization.

Functionalization with PMA. For the functionalization with PMA, 100 µL 0.05M of PMA was added to 2 mL of AuRs@SiO$_2$@IONPs ([Au] = 1mM). The solvent was evaporated in a rotary evaporator and the particles were redispersed in 1 mL of water and 100 µL of NaOH at pH = 12. The particles were washed several times until neutralization, using a magnet for separation.

Functionalization with antibodies. First, 100 µL of AuNRs@SiO$_2$@IONPs was placed in a glass vial and washed with water using a magnet for separation. Then, 200 µL of EDC (10 mM) and 100 µL (20 mM) of NHS in MES buffer were added to the NPs under sonication in a glass vial. The particles were then left for 30 min under stirring before washing twice using a magnet. Then, 10 µL of protein G (1 mg/mL) and 200 µL of PB were added and the mixture were left while stirring for 30 min; then, the NPs were washed again twice and 5 µL (1 µg), of the anti-CD44 AB (ab157107, Abcam; 559250, BD Pharmingen; or sc-7297, Santa Cruz) and 200 µL of PBS were added. The AuNRs@SiO$_2$@IONP-AB particles were washed twice again and finally redispersed in 100 µL of PBS.

Functionalization with COOH-PEG-silane. For the functionalization with COOH-PEG-silane, 1 mL of COOH-PEG-silane 1 mM was added to 2 mL of AuNRs@SiO$_2$ ([Au] = 1mM). The particles were then recovered by centrifugation and washed twice (9000 rpm – 20 min). The AuNRs@SiO$_2$ were redispersed in water.

Nanoparticles characterization.

Standard characterization. All NPs were characterized using TEM, ICP-MS, and UV-Vis. TEM images were collected with a JEOL JEM-1400PLUS transmission electron microscope operating at 120 kV, using carbon-coated 400 square mesh Cu grids. EDX Elemental maps were performed on a JEOL JEM-2100F UHR TEM operating at an acceleration voltage of 200 kV and equipped with an Oxford INCA EDX system. ICP-MS analysis was conducted using an ICP-MS Agilent 7500ce to determine the concentration of Au and Fe. Samples containing biological material (i.e., cells or spheroids) were digested in aqua regia during 48 h, followed by addition of H$_2$O$_2$ and continued heating until a clear and transparent solution was observed. The samples were cooled down to RT and subsequently measured. UV–vis optical extinction spectra were recorded using an Agilent 8453 UV–Vis diode array spectrophotometer, normalizing spectra at 400 nm or at maximum peaks.

Electron tomography of SiO$_2$@IONPs. Samples were drop casted on an amorphous carbon coated Cu TEM grid. A Thermo Fisher Scientific Themis Z electron microscope operated at a voltage of 300 kV was used, for imaging in ADF STEM mode. Hereby, the probe convergence semi-angle was 20.6 mrad, and the camera length was selected to be 73 mm resulting in inner and outer collection semi-angles of 19 and 74 mrad, respectively. Tilt series were acquired using a Fischione model 2020 tomography holder over an angular range of -75° to 60°

with a 3° tilt increment. The tilt series were reconstructed using the expectation-maximization (EM) algorithm as implemented in the ASTRA tomography toolbox.[37]

Electron tomography of AuNR@SiO$_2$@IONPs. Samples were drop casted on an amorphous carbon coated Cu TEM grid. A Thermo Fisher Scientific Themis Z electron microscope operated at a voltage of 300 kV was used for imaging in (HA)ADF STEM mode. Hereby, the probe convergence semi-angle was 20.6 mrad, and the camera length was selected to be 73 mm resulting in inner and outer collection semi-angles of 79 and 200 mrad respectively for HAADF STEM and 19 and 74 mrad for ADF STEM. Tilt series were simultaneously acquired in HAADF and ADF mode using a Fischione model 2020 tomography holder over an angular range of -70° to 66° with a 2° tilt increment. The reconstruction of the AuNR was based on HAADF STEM tilt series and the reconstruction was performed using the expectation-maximization (EM) algorithm as implemented in the ASTRA tomography toolbox[34]. To obtain a 3D reconstruction of the AuNR@SiO$_2$@IONPs, inpainting as explained by Sentosun *et al.*[38], was applied to the ADF STEM projection images. During this process, the pixels of AuNRs were removed from the ADF STEM data and replaced by the surrounding texture corresponding to SiO$_2$. The processed tilt series were then reconstructed using the EM algorithm. The 3D reconstructions of HAADF STEM and ADF STEM tilt series were then combined by using the Amira software.

Magnetism. ZFC/FC measurements were performed at 100 Oe and within a temperature range of 5-300 K, using a Quantum Design MPMS3 VSM-SQUID magnetometer with a sensitivity of 10^{-8} emu up to a maximum field of 7 T. The hysteresis loops were measured in a Vibrating Sample Magnetometer (VSM) with a sensitivity of 5·10^{-6} emu, up to a maximum field of 18 kOe working at room temperature.

Langevin and non-interacting models fitting. The standard Langevin approach to superparamagnetism (ideal SPM model) was used to provide quantitative information about the size of the particles from hysteresis loops. A non-interacting model was used to fit ZFC/FC curves. These fittings were performed as reported in previous studies.[39]

Photothermal measurements.

Photothermal measurements in solution. 50 µL aliquots of AuNRs@SiO$_2$@IONPs, SiO$_2$@4IONPs and AuNRs@SiO$_2$ at different concentrations ranging from [Au] = 0.005 - 0.1 mM ([Fe] = 0.3 - 5.2 mM) were placed in 0.5 mL Eppendorf tubes. Subsequently, they were irradiated using a multimode laser (808 nm) during 5 min at 2.5 W/cm^2 and then left for 2 min to cool down. Both heating and cooling processes were recorded using a thermal camera (FLIR SC7000) and the data were used for calculations. The procedure was repeated 3 times per sample and concentration.

SAR calculation. SAR was calculated as previously reported.[22] Briefly, the temperature elevation was measured as a function of time (dT/dt) at the initial linear slope (t = 30 s) to evaluate the heating effect in terms of SAR, power dissipation per unit mass of element, Fe or Au (W/g). SAR was calculated using the following formula where $m_{Fe/Au}$ is the total mass of Fe and Au in

the sample, m_i is the NP element mass, and C_i to the specific heat capacity of the component i:

$$SAR = \sum \frac{m_i \cdot C_i}{m_{Fe \, or \, Au}} \frac{dT}{dt}$$

Since the mass of Fe and Au are significantly lower than those of water (C_w = 4.18 J g^{-1} K^{-1}, C_{cell} = 4.125 J g^{-1} K^{-1}), the initial equation can be written as:

$$SAR = \sum \frac{m_w \cdot C_w}{m_{Fe \, or \, Au}} \frac{dT}{dt}$$

Cell culture.

2D cell culture. U87 MG human glioblastoma cells (ATCC, termed throughout as U87 cells) were cultured in Dulbecco's Modified Eagle Medium (DMEM, Gibco) supplemented with 10% fetal bovine serum (FBS, Gibco) and 1% penicillin-streptomycin (Gibco) and grown at 37 °C in a humidified incubator with 5% CO$_2$. For 2D cell experiments, cells were seeded in 96-well plates (2 x 10^4 cells/well) and allowed to adhere overnight before adding NPs, resuspended in cell media at different concentrations ([Au] = 3.1, 6.3, 12.5, and 25 μM; [Fe] = 0.16, 0.32, 0.64 and 1.3 mM), and incubating during 24h. Afterwards, the media was changed to remove the NPs that had not been internalized by the cells and fresh media was added to the cells. The cell viability was subsequently measured using the LDH and Alamar Blue assays (see below), or samples were treated for PTH using a multi-mode laser (808 nm) with 4 mm spot size, applying 12 W/cm^2 during 5 min. For irradiation experiments, NP-exposed but non-irradiated controls, in addition to non-NP exposed by irradiated cells, were included. All irradiations of 2D cell samples were conducted in the microplate with vacant wells left between samples. Post irradiation, samples were returned to the incubator and after a further 24h, cell viability tested.

2D Cell culture with NPs conjugated with antibodies. Cells were seeded in a 96-well optical imaging plate (Ibidi) and allowed to adhere. Subsequently, wells were set aside for addition of NPs (pre-conjugated with anti-CD44 antibody), or for indirect immunostaining to confirm CD44 presence. To confirm CD44 expression, cells were fixed with 4% formaldehyde and incubated with anti-human anti-CD44 (ab157107, Abcam or sc-7297, Santa Cruz, both 1/100) for 1h, followed by PBS washing, and in the case of ab157107, blocking with 1% bovine serum albumin (BSA) in PBS, and secondary AB staining using an anti-rabbit AF647 labelled secondary AB (A32795, Invitrogen). In the case of the NP-incubation wells, NPs were added at [Au] = 6.3 μM for 2h, followed by washing with PBS to remove unbound NPs. Cells were either imaged live or fixed (for AF488 and APC-CD44 labelled ABs), or in the case of indirect immunostaining samples, fixed, blocked, and subsequent secondary AB staining using A32795. In some cases, samples were counterstained with DAPI.

Confocal fluorescence microscopy. Images were taken with a Zeiss LSM 880 confocal microscope equipped with a 405 nm (Dapi), 488 nm (AF488, calcein), 561 nm (PI), and 633 nm (AF647

and APC ex) laser lines, and a multiphoton laser set at 780 nm for NP detection. For imaging, a 20x or a 40x oil immersion EC Plan-Neofluor objective was used and, in some cases, maximum intensity profiles (MIP) of z-stack images obtained to show XY, XZ, and YZ profiles of the cells. Occasionally 3-pixel mean filters were applied to remove noise pixels. 3D rendered images were conducted using ZEN software.

Cell viability assays. The AlamarBlue metabolic assay (DAL1100, Invitrogen) and CyQUANT LDH assay (Thermo) were used to measure cell viability. Briefly, following incubation with NPs, 50 μL of supernatant was removed and the LDH assay conducted following the commercial protocol. Changes in absorbance were measured at 490 and 680 nm and the percentage of cytotoxicity calculated adjusted to 100% cell death (1/10 triton X100) and 0% cell death (control cells). For the Alamar Blue assay, a solution of Alamar Blue reagent (1/10 diluted in media) was added to the cells, and after an incubation time of 2 h, fluorescence was recorded with fluorescence excitation and emission wavelengths of 570 and 585 nm, respectively. In the case that multiple timepoints were measured, the Alamar blue reagent was removed in sterile conditions and fresh media added until the following measurement, 24h, in which the above procedure was repeated. Control measurements with cells not exposed to Alamar Blue reagent at the 24h timepoint showed no change in cell viability compared to cells exposed twice to Alamar Blue, confirming the non-cytotoxic nature of this reagent.

Spheroid formation. U87 cells were seeded in 24-well plates (4 x 10^4 cells/well) and once adhered, AuNRs@SiO$_2$@IONPs (6.3 and 12.5 μM [Au], equivalent to 0.33 and 0.65 mM [Fe]) were added. After 24 h incubation, the U87 cells were detached using cell detachment solution (Sigma) and readjusted to 5.2 x 10^4 cells/mL and 150 μL/well added to Elplasia 96-well spheroid plates (Corning) to aid spheroid formation. After 72h, spheroids were collected by pipetting and irradiated in mini-Eppendorf tubes, in a total volume of 200 μL, for 5 min per sample, using a multimode laser (808 nm) with power density of 16 W/cm^2. Subsequently, spheroids were transferred back to the 96-well Elplasia plates for imaging, and the following day they were stained with Live/Dead markers (Calcein 1/250, Propidium iodide 1/50 in Hanks buffer).

Magnetic separation and PTH. Cells were plated at 4 x 10^4 cells/well in 24-well plates and the following day AuNRs@SiO$_2$@IONP-AB were added at a concentration of 6.3 μM [Au] (0.33 mM [Fe]) to one well. After 2 h, the well was stained with CellTracker DeepRed (Invitrogen, 1/200), whereas a separate well without NP incubation was stained with CellTracker Blue (Invitrogen, 1/100). After 10 min at RT, samples were washed and via cell dissociation media, cells detached. NP containing and non-NP containing cells were mixed in a total volume of 400 μL. A magnet was placed in contact with the side of the Eppendorf tube for 5 min, after which 300 μl was removed and saved as the non-NP containing cell fraction. Both this and the remaining NP containing cell fraction were centrifuged and resuspended to 50 μL for PTH irradiation. 150 μL media was subsequently added to each sample and 100 μL retained for ICP-MS analysis. The remaining 100 μL was placed

in an Ibidi 96-well optical imaging plate and allowed to adhere, with Live/Dead staining conducted the following day.

Author Contributions

C. de la Encarnación performed essential experimental work and wrote the first draft of the manuscript; F. Jungwirth performed essential experimental work; D. Vila-Liarte performed auxiliary experimental work; C. Renero-Lecuna performed auxiliary experimental work; S. Kavak performed electron tomography analysis; I. Orue performed magnetic characterisation; C. Wilhelm supported hyperthermia experiments; S. Bals performed electron tomography analysis; M. Henriksen-Lacey performed cell experiments; D. Jimenez de Aberasturi and L. M. Liz-Marzán conceived, coordinated and supervised the project. All authors revised and approved the manuscript.

Conflicts of interest

There are no conflicts to declare.

Acknowledgements

Notes and references

1   G. M. Cooper, The Development and Causes of Cancer, in: The Cell: A Molecular Approach. 2nd edition. Sunderland (MA): Sinauer Associates, 2000. Available from: https://www.ncbi.nlm.nih.gov/books/NBK9963/
2   K. Richter, M. Haslbeck, J. Buchner, *Mol. Cell* 2010, **40**, 253–266.
3   N. R. Datta, S. G. Ordóñez, U. S. Gaipl, M. M. Paulides, H. Crezee, J. Gellermann, D. Marder, E. Puric, S. Bodis, *Cancer Treat. Rev.* 2015, **41**, 742–753.
4   C. de la Encarnación, D. Jimenez de Aberasturi, L.M. Liz-Marzán, *Adv. Drug Deliv. Rev.* 2022,189, 114484
5   X. Liu, Y. Zhang, Y. Wang, W. Zhu, G. Li, X. Ma, Y. Zhang, S. Chen, S. Tiwari, K. Sji, S. Zhang, H.M. Pan, Y. X. Zhao, X-J. Liang, *Theranostics,* 2020, 10, 3793-3815.
6   C. de la Encarnación, E. Lenzi, M. Heriksen-Lacey, B. Molina, K. Jenkinson, A. Herrero, L. Colás, P. Ramos Cabrer, J. Toro-Mendoza, J. Langer, S. Bals, D. Jimenez de Aberasturi, L.M. Liz-Marzán, *J. Phys. Chem. C* 2022, **126**, 19519–19531
7   S. M. Dadfar, K. Roemhild, N. I. Drude, S. von Stillfried, R. Knüchel, F. Kiessling, T. Lammers, *Adv. Drug Deliv. Rev.* 2019, **138**, 302–32.
8   J. Chen, L. Chen, S. Du, J. Wu, M. Quan, H. Yin, Y. Wu, X. Ye, X. Liang, H. Jiang, *J. Nanobiotechnology* 2019, **17**, 116.
9   C. Liu, B. Yang, X. Chen, Z. Hu, Z. Dai, D. Yang, X. Zheng, X. She, *Nanotechnology* 2019, **30**, 285706.
10 D. L. Miyasato, A. W. Mohamed, C. A. Zavaleta, *Rev. Nanomed. Nanobiotechnol.* 2021, **13**, e1721.
11 Z. Abed, J. Beik, S. Laurent, N. Eslahi, T. Khani, E. S. Davani, H. Ghaznavi, A. Shakeri-Zadeh, *J. Cancer Res. Clin. Oncol.* 2019, **145**, 1213–1219.
12 G. González-Rubio, V. Kumar, P. Llombart, P. Díaz-Núñez, E. Bladt, T. Altantzis, S. Bals, O. Peña-Rodríguez, E. G. Noya, L. G. Macdowell, A. Guerrero-Martínez, L. M.; Liz-Marzán, *ACS Nano* 2019, **13**, 4424–4435.
13 K. Endo, T. Terada, *J. Hepatol.* 2000, **32**, 78–84.
14 M. Sanz-ortiz, K. Sentosun, S. Bals, L. M. Liz-Marzán, *ACS Nano* 2015, **9**, 10489–10497.
15 J. Park, K. An, Y. Hwang, J. E. G. Park, H. J. Noh, J. Y.Kim, J. H. Park, N. M. Hwang, T. Hyeon, *Nat. Mater.* 2004, **3**, 891–895.
16 A. Nistler, C. Hartmann, C. Rümenapp, M. Opel, B. Gleich, N. P. Ivleva, R. Niessner, M. Seidel, *J. Magn. Magn. Mater.* 2017, **442**, 497–503.
17 N. Lee, T. Hyeon, *Chem. Soc. Rev.* 2012, **41**, 2575–2589.
18 M. Knobel, W. C. Nunes, L. M. Socolovsky, E. De Biasi, J. M. Vargas, J. C. Denardin, *J. Nanosci. Nanotechnol.* 2008, **8**, 2836–2857.
19 B. S. Yadav, R. Singh, A. K. Vishwakarma, N. Kumar, *J. Supercond. Nov. Magn.* 2020, **33**, 2199–2208.
20 M. B. Mohamed, K. Z. Ismail, S. Link, M. A. El-Sayed, *J. Phys. Chem. B* 1998, **102**, 9370–9374.
21 W. J. Kennedy, S. Izor, B. D. Anderson, G. Frank, V. Varshney, G. J. Ehlert, *ACS Appl. Mater. Interfaces* 2018, **10**, 43865–43873.
22 J. Tang, M. Myers, K. A. Bosnick, L. E. Brus, *J. Phys. Chem. B* 2003, **107**, 7501–7506.
23 A. B. Serrano-Montes, D. Jimenez de Aberasturi, J. Langer, J. J. Giner-Casares, L. Scarabelli, A. Herrero, L. M. Liz-Marzán, *Langmuir* 2015, **31**, 9205–9213.
24 D. Jimenez de Aberasturi, A. B. Serrano-Montes, J. Langer, M. Henriksen-Lacey, W. J. Parak, L. M. Liz-Marzán, *Chem. Mater.* 2016, **28**, 6779–6790.
25 A. Espinosa, J. Kolosnjaj-Tabi, A. Abou-Hassan, A. Plan Sangnier, A. Curcio, A. K. A. Silva, R. Di Corato, S. Neveu, T. Pellegrino, L. M. Liz-Marzán, C. Wilhelm, *Adv. Funct. Mater.* 2018, **28**, 1803660.
26 E. Bertuit, E. Benassai, G. Meriguet, J. M. Greneche, B. Baptiste, S. Neveu, C. Wilhelm, A. Abou-Hassan, *ACS Nano* 2022, **16**, 271–284.
27 A. Espinosa, A. K. A. Silva, A. Sánchez-Iglesias, M. Grzelczak, C. Péchoux, L. Desboeufs, L. M. Liz-Marzán, C. Wilhelm, *Adv. Healthc. Mater.* 2016, **5**, 1040–1048.
28 A. Espinosa, J. Reguera, A. Curcio, A. Muñoz-Noval, C. Kuttner, A. Van de Walle, L. M. Liz-Marzán, C. Wilhelm, *Small* 2020, **16**, 1904960.
29 Q. Chen, X. Ma, L. Xie, W. Chen, Z. Xu, E. Song, X. Zhu, Y. Song, *Nanoscale* 2021, **13**, 4855–4870.
30 C. Blanco-Andujar, D. Ortega, P. Southern, S. A. Nesbitt, N. T. K. Thanh, Q. A. Pankhurst, *Nanomedicine* 2016, **11**, 121–136.
31 Q. Feng, Y. Liu, J. Huang, K. Chen, J. Huang, K. Xiao, *Sci. Rep.* 2018, **8**, 2082.
32 J. C. Fontoura, C. Viezzer, G. Fabiana, R. A. Ligabue, R. Weinlich, R. D. Puga, D. Antonow, P. Severino, C. Bonorino, *Mater. Sci. Eng. C* 2020, **107**, 110264.
33 J. Majumder, O. Taratula, T. Minko, *Adv. Drug Deliv. Rev.* 2019, **144**, 57–77.
34 C. Chen, S. Zhao, A. Karnad, J. W. Freeman, *J. Hematol. Oncol.* 2018, **11**, 1–23.
35 M. Kesik, B. Demir, F. B. Barlas, C. Geyik, S. C. Cevher, D. O. Demirkol, S. Timur, A. Cirpan, L. Toppare, *RSC Adv.* 2015, **5**, 83361–83367.
36 A. C. Marques, P. J. Costa, S. Velho, M. H. Amaral, *J. Control. Release* 2020, **320**, 180–200.

37 R. P. Castillo, M. Colilla, M. Vallet-Regí, *Expert Opin. Drug Deliv.* 2017,14, 229-243

38 W. van Aarle, W. J. Palenstijn, J. de Beenhouwer, T. Altantzis, S. Bals, K. J. Batenburg, J. Sijbers, *Ultramicroscopy* 2015, **157**, 35–47.

39 K. Sentosun, M. N. Sanz Ortiz, K. J. Batenburg, L. M. Liz-Marzán, S. Bals, *Part. Part. Syst. Charact.* 2015, **32**, 1063–1067.

40 J. Reguera, D. Jiménez de Aberasturi, M. Henriksen-Lacey, J. Langer, A. Espinosa, B. Szczupak, C. Wilhelm, L. M. Liz-Marzán, *Nanoscale* 2017, **9**, 9467–9480.